Journal of Alloys and Compounds 1037 (2025) 182617

Contents lists available at ScienceDirect

Journal of Alloys and Compounds

journal homepage: www.elsevier.com/locate/jalcom

Molecular dynamics simulation study on structure and mechanical properties of $(Ti_{41}Zr_{25}Be_{28}Fe_6)_{93}Cu_7$ bulk metallic glass

H. Vafaeenezhad [a,*], M. Haddad-Sabzevar [a], A. Rezaee-Bazzaz [a], A.R. Eivani [b]

[a] Department of Materials Science and Engineering, Engineering Faculty, Ferdowsi University of Mashhad, Azadi Square, Mashhad, Iran
[b] School of Materials Science & Engineering, Iran University of Science and Technology, Tehran, Iran

ARTICLE INFO

Keywords:
Bulk metallic glass
Molecular dynamics
Mechanical properties
Nanoindentation test

ABSTRACT

The mechanical properties of $(Ti_{41}Zr_{25}Be_{28}Fe_6)_{93}Cu_7$ bulk metallic glass were investigated using nanoindentation tests and Molecular Dynamics simulation (LAMMPS) to model the behavior of both crystalline and amorphous phases. Nanoindentation simulations employed indenter radius of 8, 10, and 15 Å, while indentation velocities of 0.1, 0.15 and 0.2 $(\frac{Å}{ps})$ were applied in both nanoindentation and tensile simulations. Nanoindentation results revealed that increasing the indentation velocity led to higher hardness in both crystalline and amorphous samples, attributed to increased applied loads at a given indentation depth. Conversely, hardness decreased with increasing indenter size. Young's modulus, a characteristic material property, remained largely unaffected by variations in indenter size and indentation velocity in both phases. Tensile simulations further confirmed that the amorphous phase exhibited superior energy absorption during deformation, likely due to its relatively inherent energy dissipation mechanisms.

1. Introduction

Bulk metallic glasses (BMG) are a new category of advanced material with a long-range disorder structure with no crystal defects like dislocation, twinning, vacancy or precipitate [1]. The BMG also known as amorphous alloys are typically formed through rapid solidification of molten metallic systems with cooling rate higher than 100 K/s [2]. Due to the exceptional atomic arrangement, such materials achieve superior mechanical characteristic, electrochemical resistance, soft magnetic properties, and tribological performance and have been extensively used in power electronics, aerospace and medical devices [3]. The Understanding and interpretation of deformation in BMGs are quite necessary for since they exhibit unique patterns from predictable crystalline metals [4] hence, several researchers have done on this topic [5–9]. It is generally believed that the local shear bands that develop from shear transformation zones (STZs) [10,11] are responsible for the inhomogeneous plastic deformation of BMGs [12,13]. Ti-based BMG are one of the most well-known amorphous alloys with good elastic limit and constrained glass forming ability (GFA) [14] and some of them are- $Ti_{45}Zr_{20}Be_{25}Ni_{10}$ [10], $Ti_{40}Zr_{25}Ni_3Cu_{12}Be_{20}$ [15] and $(Ti_{41}Zr_{25}Be_{28}Fe_6)_{93}Cu_7$ [16,17].

Nanoindentation instrumental test has been introduced as a beneficial method to study contact-based deformation patterns of BMG without needing any special sample preparation [3,11]. This nanomechanical approach has been employed in many research works to determine different properties like plastic deformation [18], creep [19], hardness [20], elasticity [21] and densification [22]. Due to intrinsic difficulty in-situ observation of the deformation progress through atomic-scale viewpoint, molecular dynamics (MD) was introduced as a powerful tool to advance understanding of deformation mechanism. MD method incorporates statistical mechanics in atomic-scale domain to investigate the nanomechanical behavior of BMG materials. Huo et al. [23] applied MD to analyze the motion routes of Li ions at presence of nucleating agent in glass-ceramic alloy considering both thermodynamics and kinetics viewpoints. The structure-mechanical properties correlation of Na_2O–CaO-Al_2O_3-B_2O_3-SiO_2 glass was studied by Lulu et al. [24] using MD with comparing the elastic modulus and fracture toughness as governing criteria in the glass network. Bogtob et al. [25] studied the progress of shear bands in Al-based BMG and focused on the role of interfaces on the atomic readjustment patterns using MD with different distribution models of atoms in the structure. Li et al. [26] studied plastic deformation and failure initiation of $Cu/Cu_{64}Zr_{36}$ amorphous composites under shock loading in presence of voids by application of MD simulation. Wang et al. [27] evaluated the effect of Y

* Corresponding author.
E-mail addresses: Hossein.vafa@gmail.com, hvafaeinezhad@um.ac.ir (H. Vafaeenezhad).

https://doi.org/10.1016/j.jallcom.2025.182617
Received 13 May 2025; Received in revised form 24 July 2025; Accepted 28 July 2025
Available online 29 July 2025

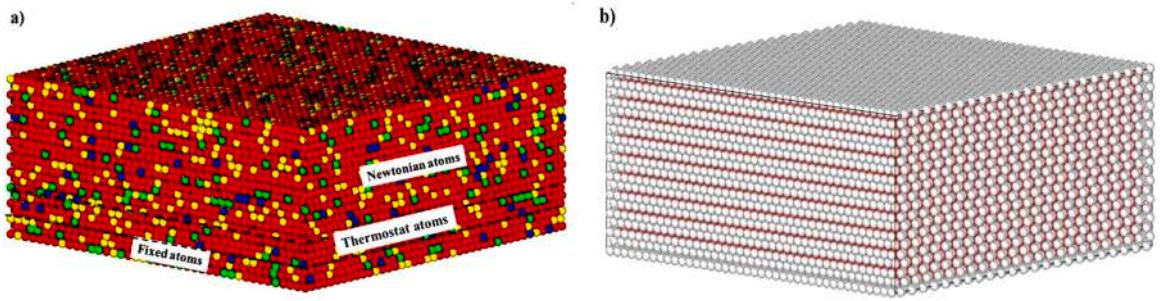

Fig. 1. (a) Md model of $(Ti_{41}Zr_{25}Be_{28}Fe_6)_{93}Cu_7$ sample created by four main atoms (red = Ti, yellow = Be, green = Zr and blue = Cu) and (b) hcp crystal structure of BMG sample.

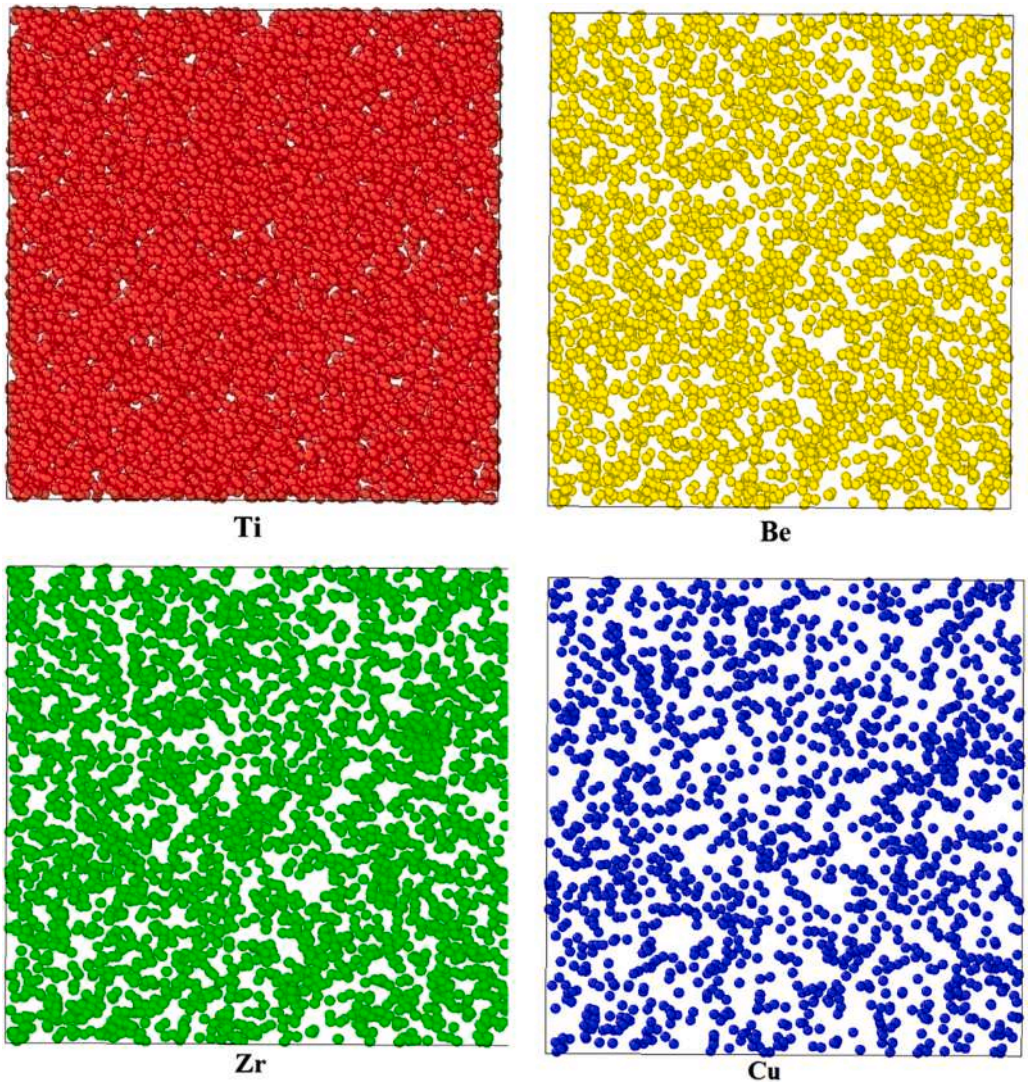

Fig. 2. The z-axis views of element distribution in amorphous sample: (a) Ti, (b) Be, (c) Zr, (d) Cu.

addition, calculation domain dimension and indenter geometry on nanomechanical behavior of the amorphous/crystalline Mg-based alloy by MD simulation. Luo et al. [28] studied the compressive and tensile mechanical properties of Zr-based BMG having different crystallization level and local shear strain orientation through structure. Celtek et al. [29] assessed glass formability and structural properties of $Zr_{50}Cu_{50-x}Al_x$ BMG by MD taking Al element addition in icosahedral ordering process into account. Annamareddy et al.[30] focused on the source of the lower activation energy of surface to bulk diffusion in $Cu_{50}Zr_{50}$ BMG and suggested that the diffusion below glass temperature can be stated as a superposition of two activated processes i.e., cage-breaking and jump barrier overcoming energies. Adjaoud et al. [31] evaluated the microstructure evolution, void closure and superficial segregation of $Pd_{80}Si_{20}$ and $Cu_{64}Zr_{36}$ alloys after cold densification by MD simulation of nano-sized BMG spheres. In this paper, MD approach is employed to study the nanomechanical behavior of $(Ti_{41}Zr_{25}Be_{28}Fe_6)_{93}Cu_7$ BMG and obtain data validated against instrumental nanoindentation experiments. The effects of loading velocity and indenter radius, on material

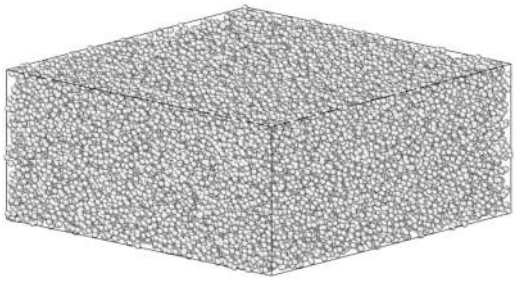

Fig. 3. Structure of BMG sample having no long-range order atomic arrangement.

Table 1
Parameters used for MD simulations of nanoindentation test in this study.

Parameter	Sample	Diamond Indenter
scale	118 × 118 × 46.86 Å	Radius 10, 15 and 20 Å
atomicity	37,660	738
Boundary conditions	p p p	-
Time step	1 fs	-
Indentation speed	0.1, 0.15 and 0.2 $(\frac{Å}{ps})$	-
Initial temperature	300 K	-

Table 2
Lennard–Jones potential coefficients between different atoms used in this study.

Pair	σ (Å)	ε (eV)	Ref.
Ti-C	3.75	0.00314	[39]
Zr-C	3.974	0.0548	[38]
Cu-Cu	2.338	0.4093	[41]
C-C	4.18	0.3050	[42]
Cu-C	3.259	0.3533	Eq.(3)

properties was systematically investigated. In addition, the tensile mechanical properties of this alloy on amorphous and crystalline state had been also simulated and the results were discussed in detail.

2. Experimental procedure

The $(Ti_{41}Zr_{25}Be_{28}Fe_6)_{93}Cu_7$ (nominal composition in at%) amorphous alloy with dimensions of 50 × 5 × 5 mm was prepared through melting of constituent elements (Ti-Zr-Be-Fe-Cu with 99.9 % purity) followed by casting in Cu mold under Argon atmosphere. In order to avoid unwanted segregation and heterogeneity, casted BMG ingot was melted three times under an inert gas atmosphere. The achieved material was examined by X-ray diffraction (Bruker – D8 advance) with Cu-K_α radiation, and transmission electron microscope (TEM)(ZEISS LEO912 microscope operating at 120 kV) was used to determine non-crystalline crystal arrangement of studied material. The instrumented nanoindentation test was performed using a Triboscope nano-indentor from Hysitron with a spherical tip connected on a contact-mode atomic force microscope (AFM).The thermal drift interference was considered less than 0.005$(\frac{nm}{s})$using a special fixture in the air media before loading step initiation [32].

2.1. Simulation method and molecular model

2.1.1. MD Simulation methodology of nanoindentation

Fig. 1(a) shows the utilized simulation model of $(Ti_{41}Zr_{25}Be_{28}Fe_6)_{93}Cu_7$ crystal sample which was created including four main elements of this alloy (e.g. Ti, Zr, Be and Cu) regarding to simplify the simulation. In addition, hcp lattice had been created with four basis atoms according to Fig. 1(b). The size of the sample was 118 × 118 × 46.86 Å in x, y and z direction respectively. Boundary conditions along all three dimensions were assumed periodic, and the time step for the simulations was set as 1 fs [33], which is very small compared to the oscillation frequency between indenter and sample atoms. As it was mentioned in many experiments before [34,35], the BMG preparation method from a crystal sample can be achieved by melting and quenching [36]. First of all, BMG was initially relaxed at 300 K, then it was heated quickly to 973 K under the heating rate of 50 K/ps to melt the sample. After that the melted sample was kept at 973 K for 1000 ps to equilibrate, followed by quenching quickly under cooling rate of 20 K/ps to initial temperature (300 K) [16]. To minimize the energy of the amorphous sample after quenching, the conjugate gradient (CG) algorithm was used for another 1000 ps. Fig. 2 represents the element distribution of the amorphous sample. As it can be seen the distribution of all elements is random [33] and there is no long-range order in the BMG sample according to Fig. 3, and the whole sample shows non-crystal structure. A rigid diamond indenter was built with a 3.57 lattice parameter and 10, 15 and 20 Å radius in order to investigate the effect of indenter size. Moreover, the indentation load was applied in z direction with a velocity of 0.1, 0.15 and 0.2 $(\frac{Å}{ps})$ in order to investigate the effect of indentation velocity in mechanical properties of BMG sample.

All the crucial parameters of MD simulation of nano indentation test are listed in Table 1.

The BMG bulk sample consisted of three kinds of atom layers; 8 Å of boundary atoms at the bottom of sample to prevent atomic motion, 8 Å of thermostat atoms with constant temperature of 300 K, and Newtonian layer atoms which obeys the classic Newton's second law. In addition, NVE microcanonical ensemble was used in both the relaxation and nanoindentation simulations steps, and OVITO software is employed to visualize the atomistic configurations [33–35].

The embedded atom method potential (eam/alloy) was used for interatomic potential between Ti, Be, Zr and Cu in BMG sample according to Eq. (1), in which the total energy E_i of an atom I is given by:

$$E_i = F_\alpha \left(\sum_{j\neq i}\rho_\beta (r_{ij})\right) + \frac{1}{2}\sum_{j\neq i}\varphi_{\alpha\beta}(r_{ij}) \quad (1)$$

where F is a function of the atomic electron density (ρ); α and β are the element types of atoms I and J, respectively; and φ denotes the pair potential interactions. EAM interatomic in-tractions potential, which was developed by Zhou et al. [37], Wang et al. [38] and Celtek et al. [33] has been extensively used and validated to liquid and amorphous systems. Its ability to adapt to heterogeneous environments and accurately handle amorphous and nanostructured phases further demonstrates its versatility for simulating a wide range of materials. Taken together, these results highlight the exceptional reliability of Zhou's EAM [37] potential for modeling complex material systems [33].

Therefore, "CuAgAuNiPdPtAlPbFeMoTaWMgCoTiZr_Zhou04.eam.alloy" potential file [37] was selected to be used in this research, and Ti considered instead of Be [39], because of their similarity in atomic radius, electronegativity, and electron density [40]. In addition, research findings reveal that in the absence of chemical interactions between atoms, long-range Vander Waals interactions can describe the interatomic interactions.Thus, the interatomic potential between indenter atoms (C) and Ti, Be, Zr and Cu atoms in substrate was modeled using the Lennard–Jones potential, with the relevant potential energy based on Eq. (2):[41]

$$E = 4\varepsilon\left[\left(\frac{\sigma}{r}\right)^{12} - \left(\frac{\sigma}{r}\right)^{6}\right] r < r_0 \quad (2)$$

where the distance between two atoms is r, r_0, σ, and ε are potential parameters, which have different constant values for different interacting atomic species.

The used lj potential coefficients in this research are listed in Table 2.

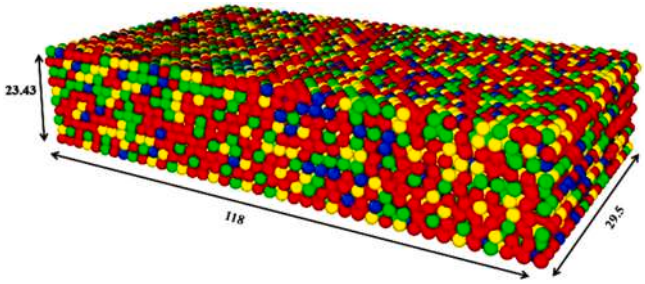

Fig. 4. The initial crystal sample created by four main atoms (red = Ti,yellow=Be,green = Zr and blue = Cu) for conducting tensile test.

Table 3
Parameters used for MD simulations of tensile test in this study.

Parameter	Sample
scale	29.5 × 118 × 23.43 Å
atomicity	16,505
Boundary conditions	s s p
Time step	1 fs
Applied force velocity	0.01, 0.015 and 0.02 $(\frac{\text{Å}}{\text{ps}})$
Initial temperature	300 K

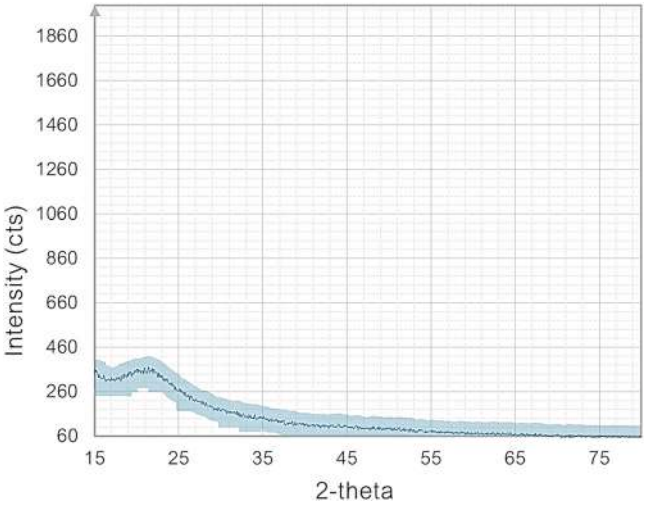

Fig. 5. XRD pattern of the as-cast$(Ti_{41}Zr_{25}Be_{28}Fe_6)_{93}Cu_7$ sample.

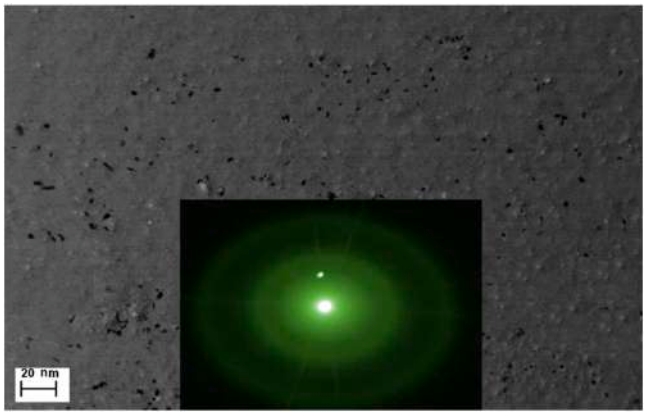

Fig. 6. TEM image and related SAED pattern of the as-cast$(Ti_{41}Zr_{25}Be_{28}Fe_6)_{93}Cu_7$ sample.

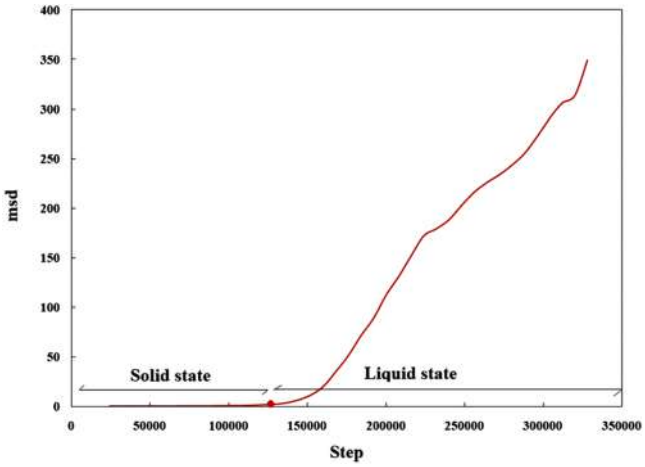

Fig. 7. Plots of msd vs. step of crystal sample during heating.

It should be mentioned that to calculate lj potential coefficient of Cu-C Lorentz-Berthelot mixing rules was used according to Eq. (3)[42], and they were listed in the last two rows of Table2.

$$\varepsilon_{A-B} = \sqrt{\varepsilon_B * \varepsilon_A} \quad , \quad \sigma_{A-B} = \frac{\sigma_A + \sigma_B}{2} \tag{3}$$

In addition, since lj potential coefficient of Be has been not developed yet, the lj potential coefficient of Ti was substituted, because between Ti, Zr and Cu atoms in chemical composition of$(Ti_{41}Zr_{25}Be_{28}Fe_6)_{93}Cu_7$, Ti has the nearest amount of atomic radius, electronegativity, and electron density to Be. These three parameters affect the lj potential coefficients of elements more strongly than other atomic properties [40].

2.1.2. Simulation of tensile test

A crystal sample with the size of 29.5 × 118 × 23.43 Å in x, y and z respectively, was produced to apply a uniaxial tensile test in y direction (Fig. 4). Then to create amorphous sample, the crystal sample was heated and quenched according to procedure which was mentioned in Section 2.1.1, and three different velocities of 0.01, 0.015 and 0.02 $(\frac{\text{Å}}{ps})$ for applying force were set at the constant temperature of 300 K to both crystal and amorphous samples. The main parameters of tensile test MD simulation are displayed in Table 3. After that, the curve of engineering stress vs. engineering strain was plotted to determine Young's modulus of each sample in different tensile velocities.

3. Result and discussion

3.1. Material characterization

The results of XRD and TEM of the as-cast sample (amorphous sample) are presented in this section. In addition, the mean-squared displacement (msd) of the group of atoms in crystal sample and the radial distribution function (RDF) also called g(r) plot extracted from MD simulation results are displayed in this section to confirm that the procedure of converting crystal sample to amorphous was applied correctly in MD simulation.

The XRD spectra of the $(Ti_{41}Zr_{25}Be_{28}Fe_6)_{93}Cu_7$ BMG material in the as-cast situation is indicated in Fig. 5. As seen,a wide-ranging extended peak appears at about $2\theta = 18^\circ$ with no high-pitched diffraction index resulting from any crystalline phase even in partial mode. The studied material is known to be homogeneous and with no long-range structural order as such lack of long-range order can in static mode be interpreted as glass structure. Fig. 6 illustrates the TEM micrograph and selected area electron diffraction (SAED) representation of the $(Ti_{41}Zr_{25}Be_{28}Fe_6)_{93}Cu_7$ sample. There exists no noticeable crystalline phase in the TEM image while the SAED outline shows a broad halo without any

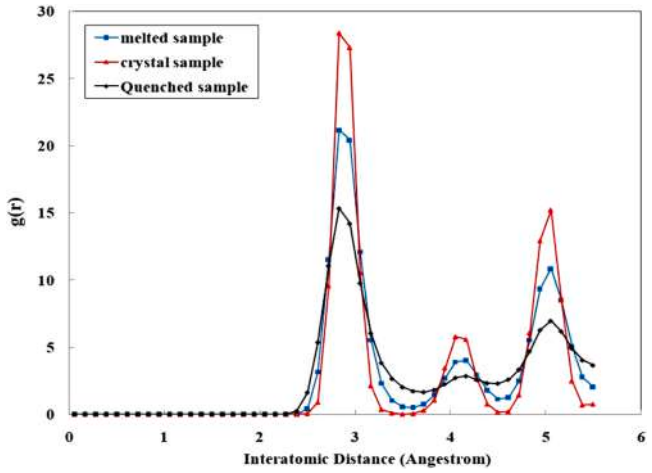

Fig. 8. Plots of partial RDF vs. interatomic distance of crystal sample, melted sample and quenched sample.

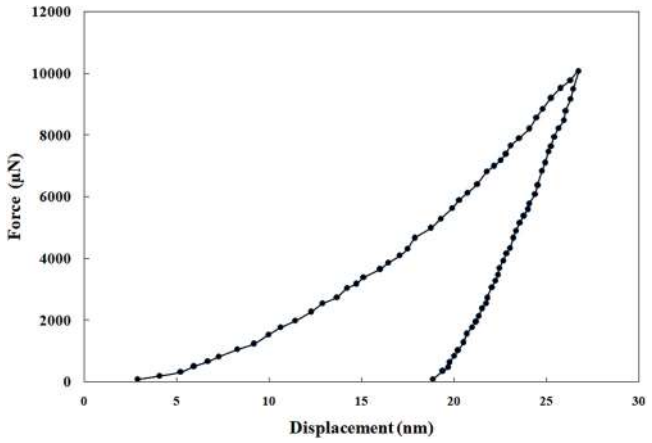

Fig. 9. load-displacement curve of BMG sample.

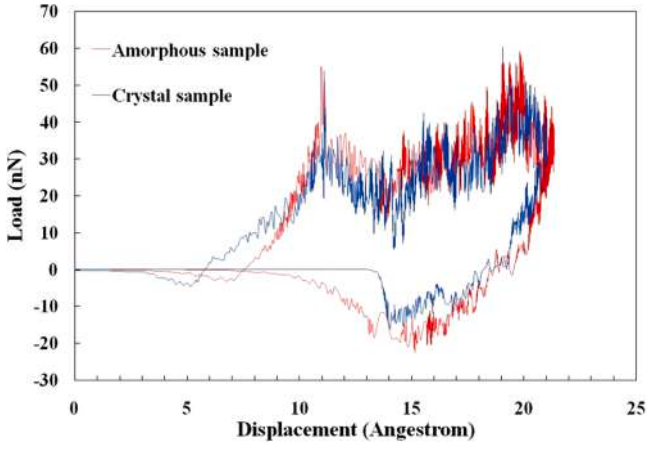

Fig. 10. The load–displacement curves at indentation velocity of 0.1 ($\frac{Å}{ps}$)with indenter radius of 1 nm for crystal and amorphous samples.

characteristic diffraction rings or spots arrangement. Hence, the microstructure of the studied alloy in the mentioned as-cast state can be considered completely amorphous.

Fig. 7 displays the mean-squared displacement (msd) of the group of atoms in crystal sample vs. step number. The slope of msd versus step

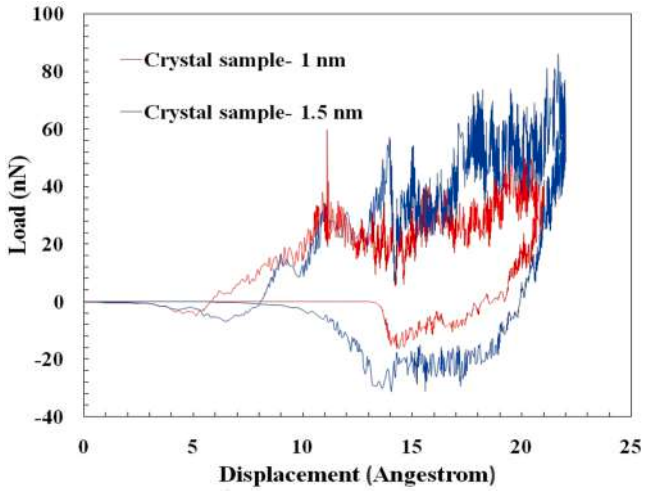

Fig. 11. The load–displacement curves of crystalline samples at indentation velocity of 0.1 ($\frac{Å}{ps}$) with different indenter radius of 1 and 1.5 nm.

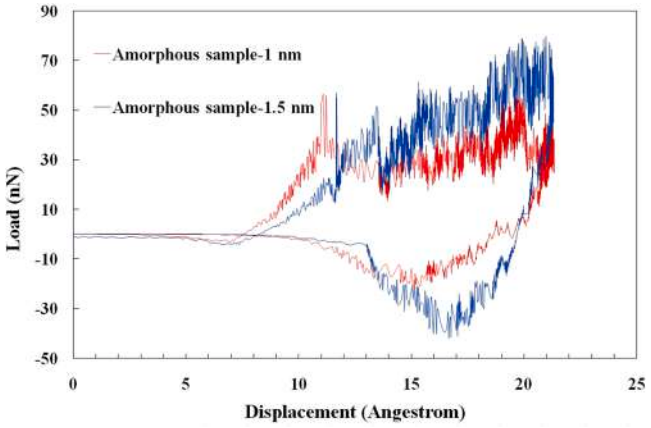

Fig. 12. The load–displacement curves of amorphoussamples at indentation velocity of 0.1($\frac{Å}{ps}$) with different indenter radius of 1 and 1.5 nm.

(temperature) is proportional to the atomic diffusion coefficient. Therefore, it can be concluded that the first part of the msd curve with the slope of zero is related to the solid state of the crystal sample, in which the atomic diffusion coefficient is almost zero. With increasing step number, and subsequently sample temperature, atomic diffusion coefficient increases, as well as the sample starts melting. Thus, the point of slope changing can be contributed to melting point of crystal sample, which was marked with a red point on the msd curve, and it equals to temperature of 970 K. Therefore, it is obvious that the crystal sample was melted at 970 K, and after quenching with high cooling rate, it is converted to an amorphous sample which is in accordance with previous researches [16,17].

Fig. 8 shows the radial distribution function (RDF) also called g(r) plot, and the coordination number for a group of particles in crystal sample, melted sample, and quenched sample. The RDF explains the distribution of distance between atoms, which provides atomic scale structural information, and displays the short-range order (SRO)in the material [38]. There are three distinct and sharp peaks, which characteristic of crystal structure of materials, in interatomic distances of 3, 4 and 5 Å. These interatomic distances represent the probability of finding an atom at a certain distance from another atom, in other words, it is a representative of the existence atomic order in the structure of materials. As it can be inferred from Fig. 8, with increasing temperature of crystal sample, the distance between atoms increases in the melted sample,

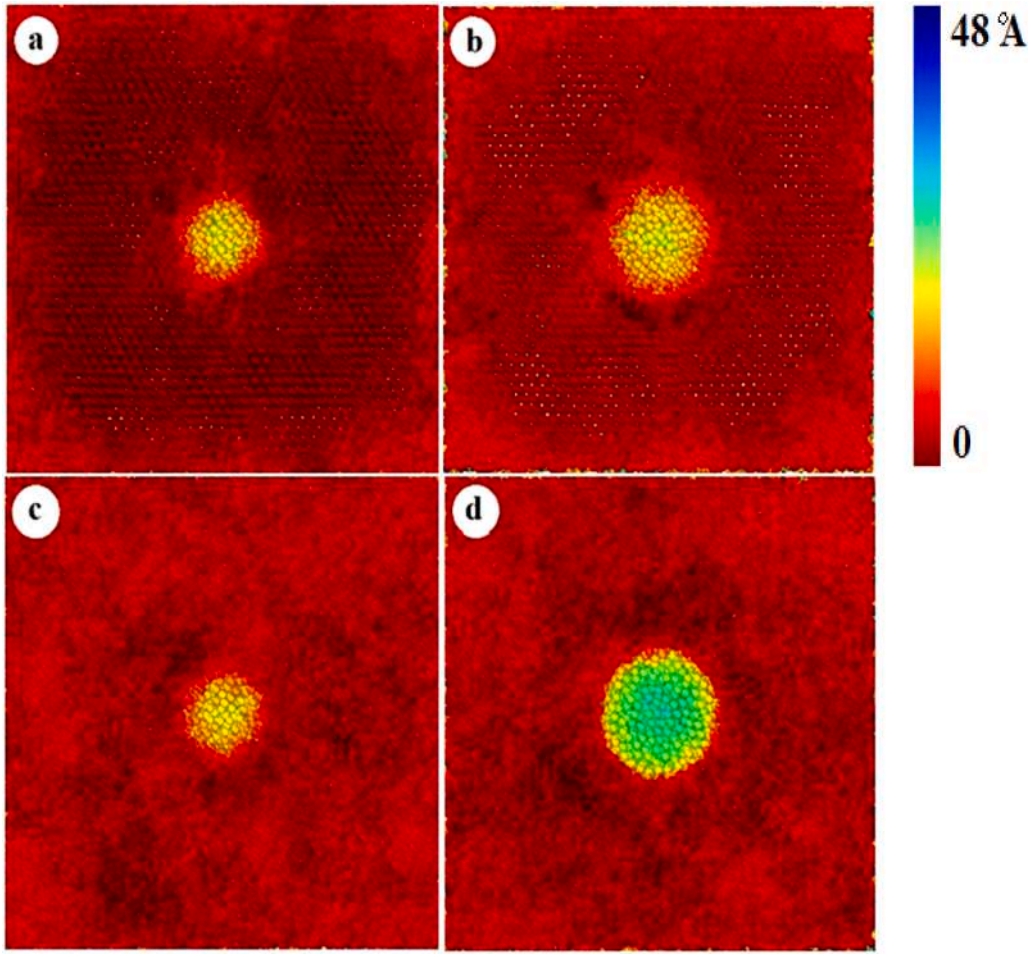

Fig. 13. The xy plane view of (a,b) crystal samples, and amorphoussamples (c,d) at indentation velocity of 0.1($\frac{Å}{ps}$) with different indenter radius of 1 and 1.5 nm.

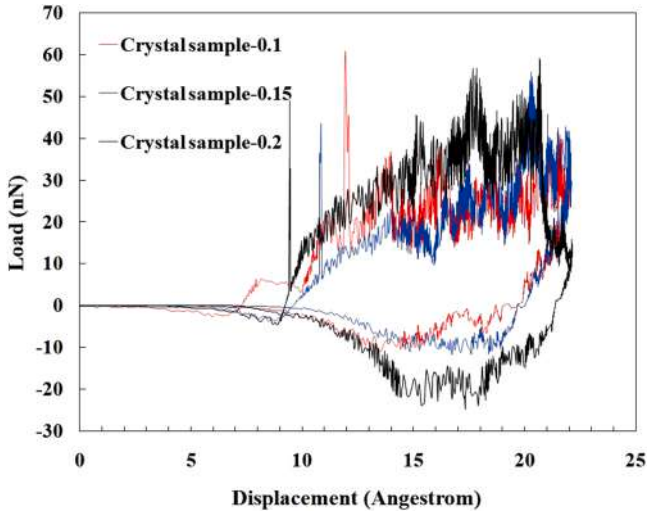

Fig. 14. The load–displacement curves of crystal samples with indenter radius of 0.8 nm and at different indentation velocity of 0.1,0.15, and 0.2 ($\frac{Å}{ps}$).

subsequently the intensity of peaks reduces, and they are a bit broadened. After quenching the melted sample with the cooling rate of 20 K/ps, an amorphous sample was built without a long-range order of atoms, leading to reducing the peaks intensity and disappearing the second peak.

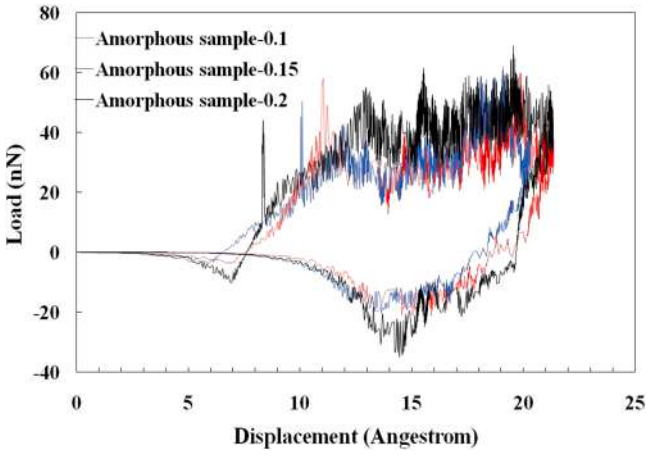

Fig. 15. The load–displacement curves of amorphous samples with indenter radius of 0.8 nm and at different indentation velocity of 0.1,0.15, and 0.2 ($\frac{Å}{ps}$).

3.2. *Nanoindentation test results*

To have a good comparison between a real nanoindentation test and MD simulation result, a nanoindentation test was applied on the surface of the amorphous sample, and the amount of hardness and Young's modulus of the amorphous sample was calculated to be compared with MD simulation results. Fig. 9 represents the load-displacement curve of

Table 4
The properties of crystalline and amorphous samples calculated by MD simulations.

Property	Crystal sample						Amorphous sample					
	H (Gpa)			E (Gpa)			H (Gpa)			E (Gpa)		
Indenter radius (Å)	8	10	15	8	10	15	8	10	15	8	10	15
Indentation velocity = 0.1 ($\frac{Å}{ps}$)	7.5	7.15	6.75	112	115	120	6.6	6.2	5.8	109	112	117
Indentation velocity= 0.15($\frac{Å}{ps}$)	7.8	7.4	6.9	118	122	124	6.9	6.3	6	111	120	121
Indentation velocity= 0.2($\frac{Å}{ps}$)	7.95	7.8	7.3	122	125	129	7.2	7	6.4	117	123	127

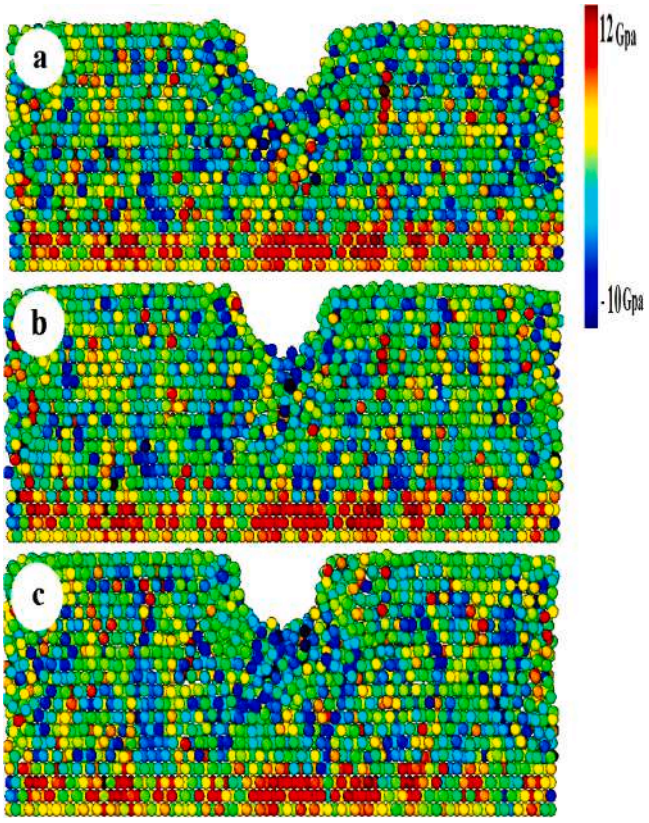

Fig. 16. Stress distribution across xz plane of crystal samples under conducting nanoindentation test with indenter radius of 0.8 nm and a) loading velocity of 0.1($\frac{Å}{ps}$),b) 0.15($\frac{Å}{ps}$). and c)0.2($\frac{Å}{ps}$).

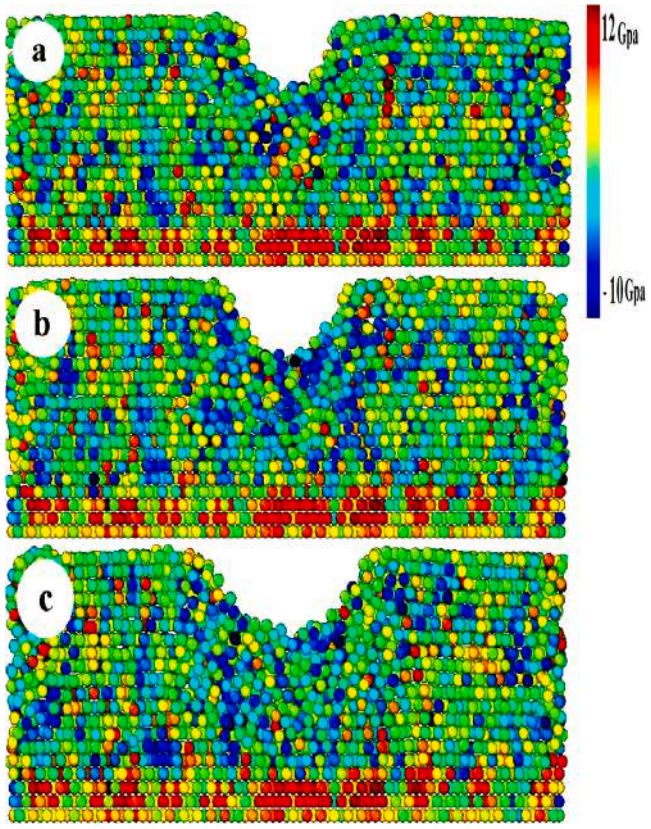

Fig. 17. Stress distribution across thexz plane of crystal samples under conducting nanoindentation test with loading velocity of 0.1($\frac{Å}{ps}$).and a) indenter radius of 0.8 nm, b) 1 nm, and c) 1.5 nm.

amorphous sample obtained from a real nanoindentation test indentation velocity of 0.25 ($\frac{\mu N}{s}$).The maximum applied force in the nanoindentation test was 10×10^3 μN, and the penetration depth of the spherical indenter on the surface of the sample was about 27 nm. Fig. 9 provides critical understanding of material's elastic and plastic properties. The load-displacement curve includes loading and unloading steps, and its shape has effect on hardness (H) and Young's modulus (E) of material [43,44]. During loading, the indenter penetrates the material, and the curve reflects both elastic and plastic deformation.While unloading curve reflects elastic recovery, and its necessity for extracting Young's modulus. The slope of unloading curve reflects elastic recovery, and it is used to calculate (E) via the Oliver-Pharr method.To calculate material mechanical properties such as hardness and Young's modulus values for all the load-displacement curves in this research, Oliver and Pharr method has been used. The hardness H is defined as the material's resistance against local plastic deformation, which was calculated according to Eq. (4) [45]

$$H = P_m / A_c \tag{4}$$

A_c is the projected contact area on the surface of the sample after conducting a nanoindentation test, and it was 2689.180 nm^2.

Moreover, S which represents the contact stiffness in the unloading curve at h_{max} is calculated according to Eq. (5) [45]

$$S = \left(\frac{dP}{dh} \right)_{h=h_{max}} \tag{5}$$

Eq. (6) and (7) are used to obtain the amount of Young's modulus (E) using nanoindentation test results.

$$\frac{1}{E_r} = \frac{1-\nu_i^2}{E_i} + \frac{1-\nu^2}{E} \tag{6}$$

$$E_r = \frac{\sqrt{\pi}}{2\beta} \frac{S}{\sqrt{A_c}} \tag{7}$$

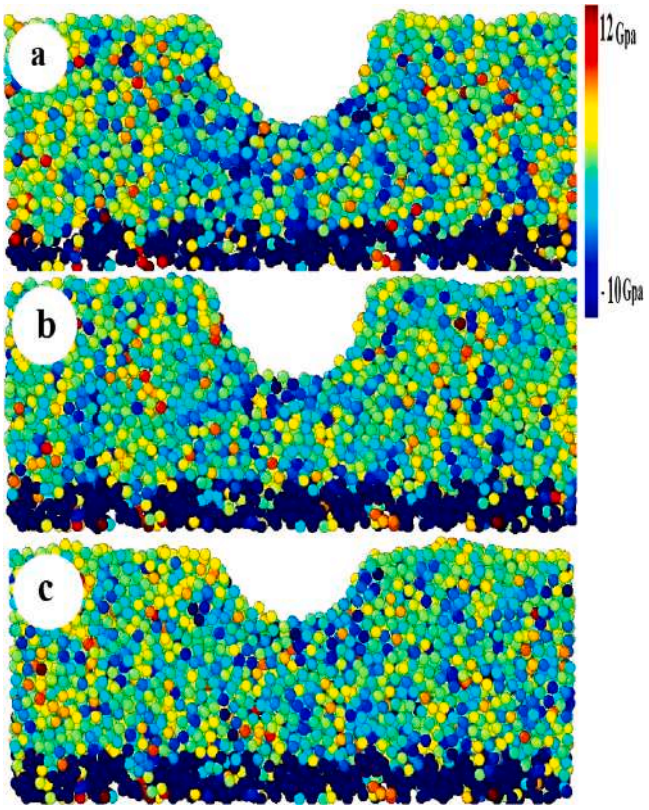

Fig. 18. Stress distribution across the xz plane of amorphous samples under conducting nanoindentation test with indenter radius of 1.5 nm and a) loading velocity of 0.1($\frac{\text{Å}}{ps}$), b) 0.15($\frac{\text{Å}}{ps}$), and c) 0.2($\frac{\text{Å}}{ps}$).

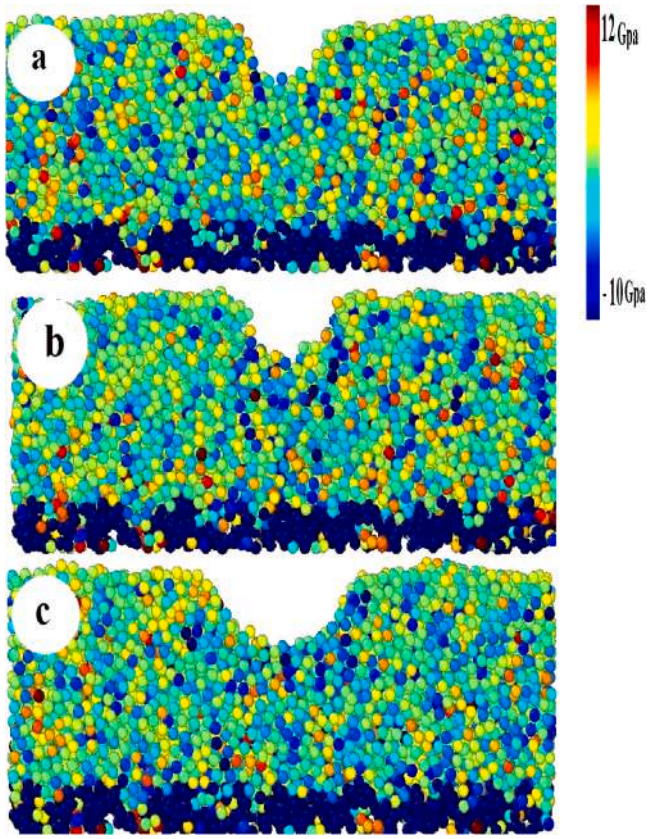

Fig. 19. Stress distribution across the xz plane of amorphous samples under conducting nanoindentation test with loading velocity of 0.2 ($\frac{\text{Å}}{ps}$), and a) indenter radius of 0.8 nm, b) 1 nm, and c) 1.5 nm.

where E_i= 1141 GPa (the Young's modulus of the diamond indenter),ν_i= 0.11 (Poisson's ratio of the diamond indenter), $\beta = 1$ (a constant related to indenter shape), $\nu = 0.32$ (the Poisson's ratio of the crystal sample), and $\nu = 0.36$ (the Poisson's ratio of the amorphous sample during elastic deformation) [46]. Considering Eq. (4)–(7), the amount of hardness and Young's modulus of $(Ti_{41}Zr_{25}Be_{28}Fe_6)_{93}Cu_7$ amorphous sample had been calculated 6.7Gpa and 118Gpa respectively, which are in good agreement with previous paper.

In addition, nanoindentation tests on the surface of crystal and amorphous samples, had been simulated using LAMMPS, and the load-displacement curve, stress distribution across the sample and atomic position of samples after conducting nanoindentation test had been investigated.To compare the response of $(Ti_{41}Zr_{25}Be_{28}Fe_6)_{93}Cu_7$ crystal and amorphous samples in nanoindentation test, load-displacement curves of both of the samples under the same situation (Indenter radius= 10 Å, indentation velocity = 0.10 ($\frac{\text{Å}}{ps}$)) was plotted in Fig. 10. Although simulated nanoindentation test was conducted in displacement control mode, indentation depth of amorphous samples is a bit larger than crystal samples [47] (as the experienced force in Fig. 10 in both samples is almost equal), which means amorphous sample has smaller amount of hardness compared with crystal sample. However, Fig. 10 reveals that the area under the load-displacement curve for amorphous samples is a bit bigger than that of crystal samples. It should be considered that MD simulated results are not reliable to compare material's toughness because it has some methodological limitations, and it does not consider microstructural complexities of materials due to too localized testing zone [48]. Previous studies confirmed that amorphous sample absorbs more energy during deformation, because amorphous material such as BMGs often experience homogeneous plastic flow, which causes easier atomic rearrangement and energy absorption [49,50].

Fig. 11 represents the load vs. displacement curves of $(Ti_{41}Zr_{25}Be_{28}Fe_6)_{93}Cu_7$ crystal samples under constant indentation velocity (0.1 ($\frac{\text{Å}}{ps}$))with different radiuses of indenter (1 and 1.5 nm). It is observed that when the diamond indenter gradually moves down in z direction and in a distance of about 3 Å for both sizes of indenters, an adsorption phenomenon can be seen. In these moments, the indenter is subjected to a negative force, which shows adsorption force between the sample and indenter. However, with increasing the indenter radius, the area of adsorption phenomenon increases as well [45,51]. In addition, although the diamond indenter with larger radius at constant indentation velocity and indentation depth, experiences larger force, previous researches confirmed that the hardness of samples reduced with increasing the indenter radius. It can be attributed to the larger contact area of bigger indenter with the sample, which applies the force over a larger volume of samples, reduces localized stress, and reduces hardness value. Conversely, the sharper indenter (with lower indenter radius) concentrated stress over a smaller area which led to bigger value of stress, and larger value of hardness. The same trend has been observed for conducting nanoindentation test on the surface of $(Ti_{41}Zr_{25}Be_{28}Fe_6)_{93}Cu_7$ amorphous sample with different indenter radius (1 and 1.5 nm), and the relevant results were indicated in Fig. 12. Simulated profilometer of the crystal and amorphous sample surfaces after indentation is shown in Fig. 13. This illustration confirms the fact that increasing the radius of diamond indenter, cause increasing in the contact area, and indentation depth samples.

Another attempt of this research is investigation of the effect of indentation velocity in the mechanical properties of $(Ti_{41}Zr_{25}Be_{28}Fe_6)_{93}Cu_7$ crystal and amorphous samples. The load-displacement curves of crystal and amorphous samples with indenter radius of 0.8 nm at different indentation velocities of 0.1,0.15 and 0.2 ($\frac{\text{Å}}{ps}$) was

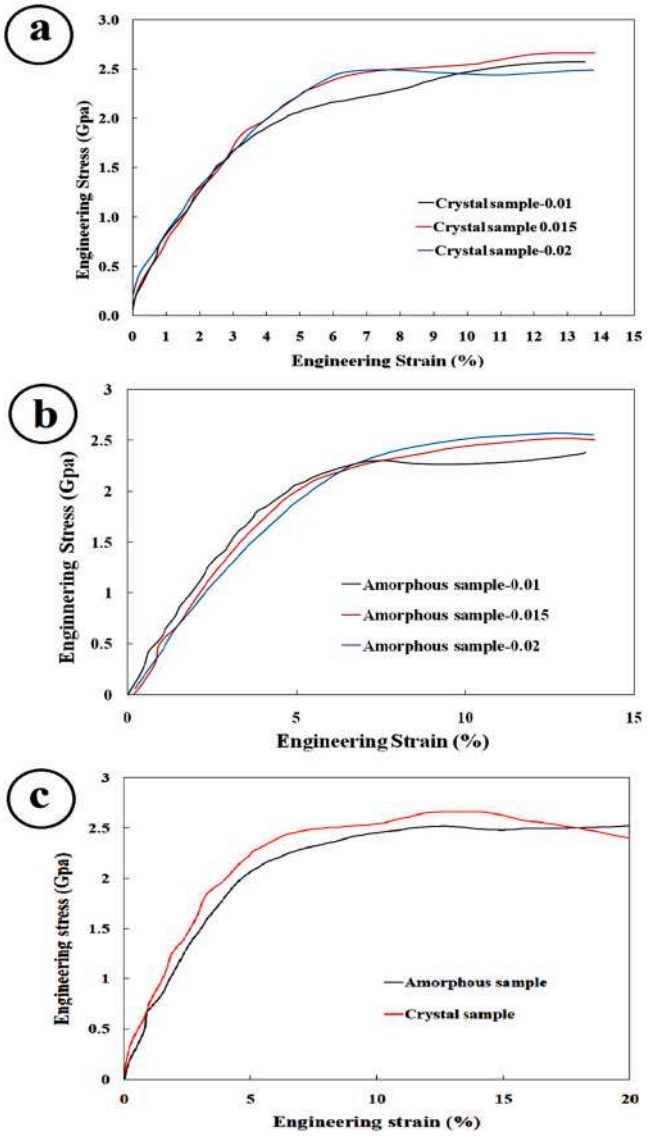

Fig. 20. Engineering stress vs. engineering strain plots for a) crystal b) amorphous samples under different velocities of applying load, and c) crystal and amorphous samples at constant velocity of 0.02 ($\frac{\text{Å}}{ps}$).

Table 5
Calculated Young's modulus of crystal and amorphous samples under different velocity.

State	0.01($\frac{\text{Å}}{ps}$)	0.015($\frac{\text{Å}}{ps}$)	0.02($\frac{\text{Å}}{ps}$)
Crystal sample	110	107	104.5
Amorphous sample	105	101.5	97

plotted in Figs. 14 and 15. As it can be seen, increasing indentation velocity has the same effect on crystal and amorphous samples, so that with increasing the indentation velocity, the sample showed bigger hysteresis loop, in addition, higher applied loads in the same indentation depth have been observed for both samples when the indentation velocity was 0.2 ($\frac{\text{Å}}{ps}$). Thus, it can be concluded that strain rate sensitivity (SRS) of these sample is positive [52], which will be studied in Section 3.4. Since the MD simulation of nanoindentation test has been performed in displacement control mode, the effect of indentation velocity on indentation depth has not been discussed. Moreover, increasing

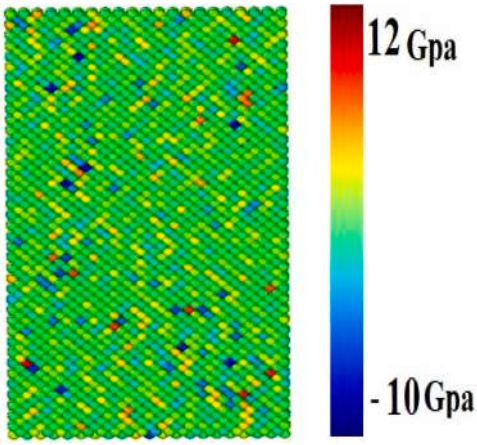

Fig. 21. Stress distribution of xy plane of initial crystalline sample.

indentation velocity caused to occurrence of pop-in in curves to the bigger indentation depth [52]. As a result, pop-in was in 13.5, 14 and 14.75 Å for crystal samples at the indentation velocities of 0.1, 0.15 and 0.2 ($\frac{\text{Å}}{ps}$),respectively. Similarly, pop-in was in 11, 12 and 13 Å for amorphous samples at the indentation velocities of 0.1, 0.15 and 0.2 ($\frac{\text{Å}}{ps}$), respectively. In addition, increasing the indentation velocities has an effect on the area of adsorption phenomenon, and the adsorption area increased with increasing indentation velocity in both crystal and amorphous samples.

To calculate material's mechanical properties such as hardness and Young's modulus values for all the curves, Oliver and Pharr method has been used according to Eqs. (4)–(7). Other equations to be used in simulation result plots are as follows: [35,46]

$$A_c = \pi\,(2R\text{-}h_c)\,h_c \tag{8}$$

A_c is the projected contact area, and it relates to R (the indenter radius) and h_c (the projected contact depth).Moreover, $h_c$can be calculated according to Eq.9, in which ε equal to 0.75 for a spherical indenter. [35,46]

$$h_c = h_{max} - \varepsilon\frac{Pmax}{S} \tag{9}$$

Considering Eq. (4)–(9), the amount of hardness and Young's modulus of $(Ti_{41}Zr_{25}Be_{28}Fe_6)_{93}Cu_7$ crystal and amorphous samples under different indenter radius and indentation velocities had been calculated and they were listed in Table 4.

As it is obvious, calculated hardness andYoung'smodulus from real nanoindentation test for an amorphous samplewhich is reported before (6.7 and 118 Gpa), is in good agreement with the average amount of H and G for amorphous samples in Table 4 (6.48 and 117.4 Gpa).In addition, there are a good agreement between calculated hardness and Young's modulus values of amorphous samples with previous research [16] which was reported 7.95 and 120 Gpa for hardness and Young's modulus respectively.

Stress distribution of crystal samples across xz plane under conducting nanoindentation test with indenter radius of 0.8 nm and different loading velocities of 0.1, 0.15 and 0.2($\frac{\text{Å}}{ps}$)was shown in Fig. 16. In all crystal samples some atom layers had been fixed in the bottom of samples, and they experienced tension stress from 2.45 to 12 Gpa. Moreover, while indenter penetrates into sample, compression stress is applied in the atoms of samples especially around the indenter, which according to Fig. 16 maximum compression stress is −10 Gpa. In Fig. 16 atoms had been colored from blue to red, which represents compression stress and tension stress respectively. In addition, conducting nanoindentation tests with bigger loading velocity 0.2($\frac{\text{Å}}{ps}$) at constant

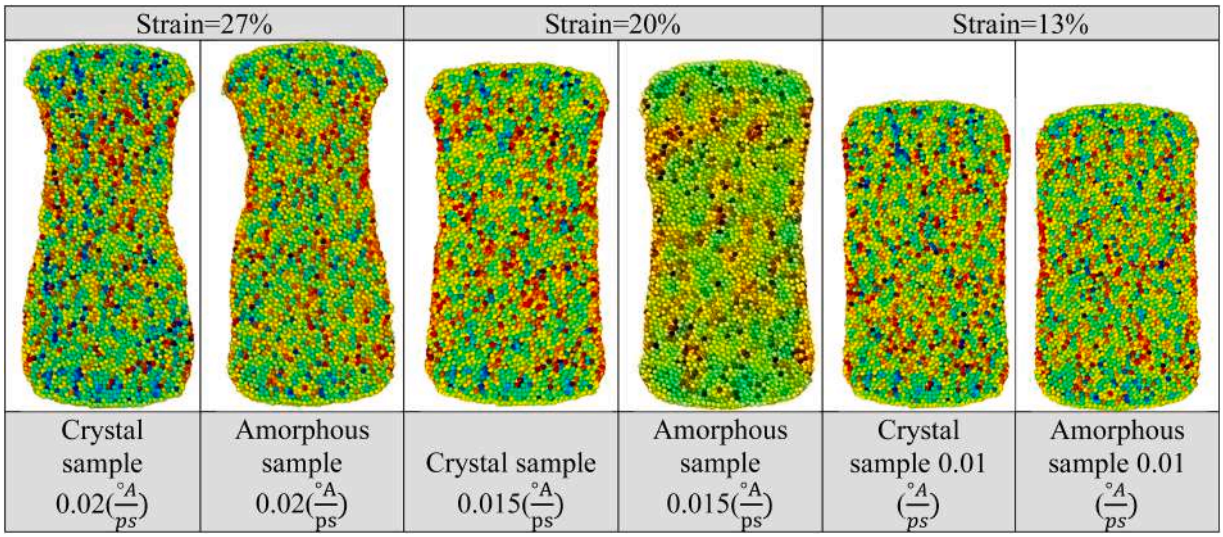

Fig. 22. Stress distribution across xy plane of crystal and amorphous samples after conducting tensile test with different parameter.

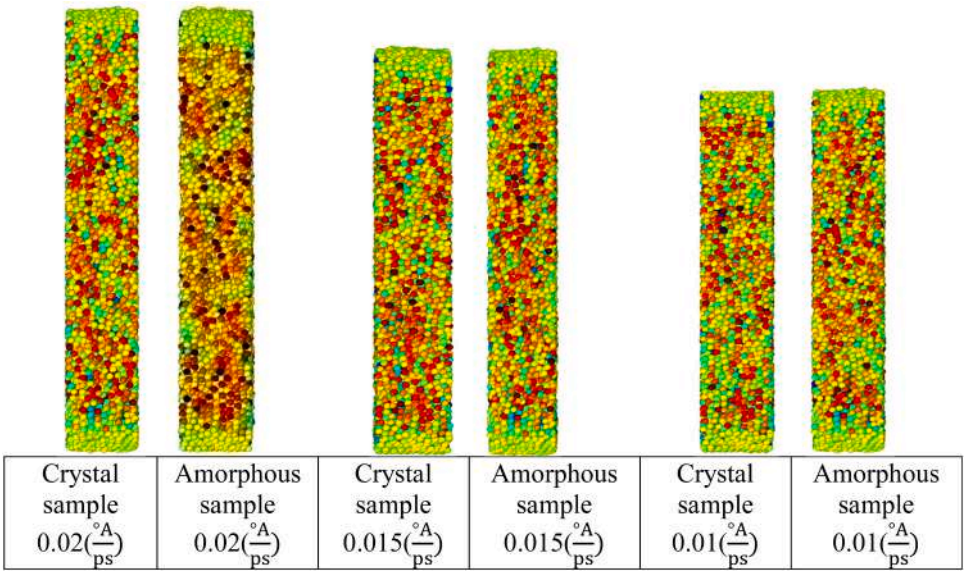

Fig. 23. Stress distribution across zy plane of crystal and amorphous samples after conducting tensile test with different parameter.

indenter radius, applied compression stress in more atoms around indenter, which caused higher sample hardness, as it was mentioned in Table 4.

On the other hand, the effect of indenter radius on the stress distribution of crystal samples across thexz plane was illustrated in Fig. 17.As it was expected from Fig. 17 and Table 2, increasing the indenter radius gave rise to escalating contact area between sample and the indenter, decreasing hardness of samples, and increasing the number of atoms which withstand compression stress. Due to all of the above-mentioned observations, as Fig. 17 and Table 2 displayed before, the hardness of $(Ti_{41}Zr_{25}Be_{28}Fe_6)_{93}Cu_7$ crystal samples decreased with increasing the indenter radius at the constant strain rate.

The same investigation has been applied in the distribution of stress across the xz plane of $(Ti_{41}Zr_{25}Be_{28}Fe_6)_{93}Cu_7$ amorphous samples, and the results have been shown in Figs. 18 and 19. In comparison with Figs. 16 and 17 which showed the same figures for crystal samples, it can be said that the general distribution of stress across the xz plane is inhomogeneous in crystal and amorphous samples. Most of the atoms in amorphous samples experienced lower range of stress, which is mainly compressive stress, and a smaller number of atoms experienced tensile stress in amorphous samples. The more uniform stress distribution in amorphous samples compared with the crystal ones, results in homogeneous deformation, which is known as energy absorption mechanism in amorphous material, and lead to higher energy absorption during deformation which confirmed by previous research [18,53]. Furthermore, some layers of atoms which had been fixed in the bottom of samples, were colored in blue, which represented compression stress unlike crystal samples.

3.3. Tensile test results

MD simulation of tensile test of the crystal and amorphous samples had been conducted, and the amount of calculated Young's modulus was compared with the results of nanoindentation test.Fig. 20 (a–c) represents the flow curves of crystal and amorphous samples under different velocities of applying load of 0.01, 0.015 and 0.02 ($\frac{Å}{ps}$), It is obvious that in both samples, increasing velocities of applying load shifts the stress-strain curves to an upper amount of stress, which was proved by previous researches [18,52,54]. The value of Young's modulus was

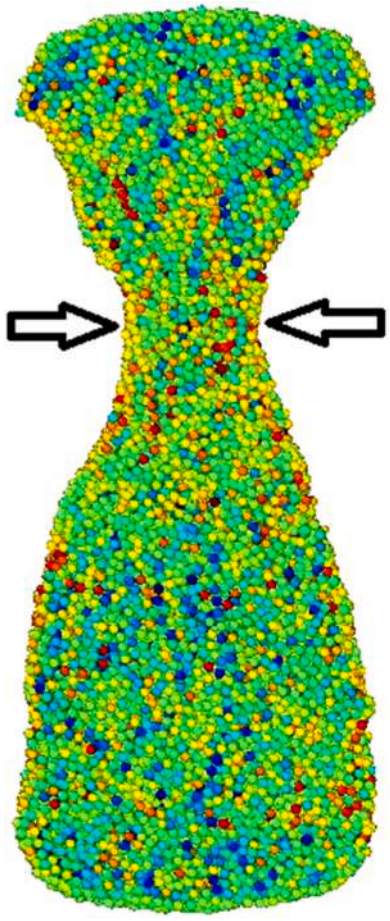

Fig. 24. Stress distribution and necking zone across xy plane of amorphous sample after conducting tensile test with strain of 73 % and velocity of 0.02($\frac{Å}{ps}$).

calculated by fitting a line on the linear part of each graph and obtaining its slope, which is almost constant with increasing velocities of applying load in each sample. This contributed to the fact that Young's modulus is a characteristic parameter of each material, and it is not affected by increasing the strain rate. In addition, Fig. 20-c shows the flow stress curves of amorphous and crystal samples at constant velocity of 0.02 ($\frac{Å}{ps}$). It can be inferred that, crystal sample showed higher amounts of Young's modulus due to long range order, whereas random distribution of atoms in the amorphous sample led to lack of order which means the transmission of stress is less efficient [55]. Higher Young'smodulus of crystal sample indicates high resistance to deformation which is typical for material with a lattice structure. In contrast, amorphous materials lack long-range order, which leads to lower elastic moduli. Determined values of Young's modulus of each curve are presented in Table 5. Furthermore, the amount of engineering stress of crystal samples started to decrease around engineering strain of 15 %, whereas the amount of engineering stress of amorphous samples stayed constant. In the previous research conducting in situ tensile tests in a transmission electron microscope was confirmed that metallic glasses showed large tensile ductility in the range of 23–45 %, in addition, significant uniform elongation and extensive necking was reported [56], which are in good agreement with results presented in Figs. 20 and 24.

This phenomenon can be attributed to the fact that amorphous materials can tolerate more energy during deformation as it was mentioned in Section 3.1, and they usually experience homogeneous plastic flow which was reported in similar study [49].

Fig. 21 shows the stress distribution across the xy plane of crystal samples before conducting a tensile test, and it showed uniform stress distribution in the sample. To have better judgment, the stress color bar was kept in a constant range of −10 to 12 GPa in Figs. 22–24.

To observe thestress localization after conducting tensile tests in crystal and amorphous samples under different strain rates, the stress distribution around each atomic site is calculated, as shown in Fig. 22using OVITO software. According to the figure, samples experience different amounts of total strain, because the number of steps to apply deformation was assumed constant. Therefore, sample experience 13, 20 and 27 % of strain in strain rate of 0.01, 0.015 and 0.02 ($\frac{Å}{ps}$) respectively. At strain of 13 %, both samples showed homogeneous deformation and stress localization), while at higher strain rates (0.015 and 0.02 ($\frac{Å}{ps}$), samples showed heterogeneous deformation and stress localization, especially in the edges of the sample and in y direction. To have better vision of stress distribution in the sample thickness, the yz plane of samples in the last step of the tensile test are shown in Fig. 23. Lots of atoms which are colored with red, experience large amounts of tensile stress around 12 GPa, while there are atoms which experience compression stress (around −10 GPa), and they generally exist in the top and bottom of the sample. These areas are contributed to fixed parts of the sample, the same as grip lengths of the sample in the real tensile test. Moreover, when samples showed 20 and 27 % of strain, their shape changed from rectangle to dumbbell-shaped, because the samples width decreased, their length increased, and the necking began to happen, since it was reported that during tensile test,the majority volume of BMG samples does not participate to plastic deformation, and severe strain localization happened in samples and the necking zone creates[56].To have a better view of necking in crystal and amorphous samples, tensile tests were conducted till strain of 73 %, and the stress distribution and necking zones of the amorphous sample are presented in Fig. 24 [38].

3.4. Strain rate sensitivity (SRS) calculation

In order to determine the amount of SRS for $(Ti_{41}Zr_{25}Be_{28}Fe_6)_{93}Cu_7$ crystal and amorphous samples, flow stress curve of these materials under different strain rate was used (Fig. 20(a,b)). The value of SRS is obtained from Eq. 10, where σ is stress and $\dot{\varepsilon}$ in relevant strain rate:[36, 54]

$$SRS = \frac{\partial \ln \sigma}{\partial \ln \dot{\varepsilon}} \tag{10}$$

The amount of strain rate in MD simulation of tensile test can be achieved by Eq. (11), where v is the velocity of tensile test andL_0 is the initial length of samples which equals 118 Å in this research. Therefore, the amount of strain rates for velocities of 0.01, 0.015, and 0.02($\frac{Å}{ps}$) can be determined based on Eq. (11): [52]

$$\dot{\varepsilon} = \frac{v}{L_0} \tag{11}$$

With plotting the amount of $\ln(\dot{\varepsilon})$ vs. ln(σ)and fitting a linear equation on the curves, the amount of SRS is obtained as the slope of the lines. These values are 0.14 and 0.012 for crystal and amorphous samples respectively. Research findings reveal that MD studies for most BMG reported positive SRS [54]. Also, the obtained positive values for crystal and amorphous samples, again confirmed that increasing velocity in nanoindentation test resulted in bigger hysteresis loop, in addition, higher applied loads in the same indentation depth for both samples.

4. Conclusions

Simulation of nanoindentation and tensile test on crystal and amorphous samples of $(Ti_{41}Zr_{25}Be_{28}Fe_6)_{93}Cu_7$ was conducted, and the results are as follow:

1. Simulation and experimental results of nanoindentation tests on amorphous samples are in good agreement.

2. Increasing indentation velocity in nanoindentation tests of crystal and amorphous samples led to increasing hardness, because of higher applied loads in the same indentation depth for both samples. But increasing indenter size causes decreasing hardness, due to the larger contact area of bigger indenter with the sample, and consequently reduces localized stress.
3. Simulation of a tensile test showed that amorphous samples can tolerate more energy during deformation due to energy absorption mechanism in amorphous materials.
4. As it was expected from increasing the amount of hardness with increasing the indentation velocity in both samples, the amount of SRS for crystal and amorphous was positive, and it had been calculated 0.14 and 0.012 respectively.

CRediT authorship contribution statement

A.R. Eivani: Writing – review & editing, Software, Conceptualization. **H. Vafaeenezhad:** Writing – original draft, Methodology, Investigation, Formal analysis, Data curation, Conceptualization. **A. Rezaee-Bazzaz:** Writing – review & editing, Resources, Project administration. **M. Haddad-Sabzevar:** Software, Resources, Investigation.

Declaration of Competing Interest

The authors have declared no conflict of interest.

References

[1] G. Cao, et al., Melt fluidity and microstructure of bulk metallic glass under different cooling conditions, J. Alloy. Compd. 1015 (2025) 178869.
[2] A. Fadhil, et al., Low temperature plasticity maximum in a Zr-Cu-Ni-Al bulk metallic glass, J. Alloy. Compd. 1017 (2025) 179085.
[3] P. Tao, et al., Nanoindentation and relaxation behavior of nitrogen doped zirconium based bulk metallic glass, J. Alloy. Compd. 999 (2024) 174983.
[4] Z. Wu, et al., Effect of Nb on the mechanical properties and toughening mechanism of Zr-Co-Al(-Nb) bulk metallic glasses, J. Alloy. Compd. 984 (2024) 173971.
[5] J. Eckert, et al., Mechanical properties of bulk metallic glasses and composites, J. Mater. Res. 22 (2) (2007) 285–301.
[6] H. Li, Y. Zheng, Recent advances in bulk metallic glasses for biomedical applications, Acta Biomater. 36 (2016) 1–20.
[7] J.F. Löffler, Bulk metallic glasses, Intermetallics 11 (6) (2003) 529–540.
[8] B. Sun, W. Wang, The fracture of bulk metallic glasses, Prog. Mater. Sci. 74 (2015) 211–307.
[9] M.M. Trexler, N.N. Thadhani, Mechanical properties of bulk metallic glasses, Prog. Mater. Sci. 55 (8) (2010) 759–839.
[10] S. Zhao, et al., Quaternary Ti–Zr–Be–Ni bulk metallic glasses with large glass-forming ability, Mater. Des. 85 (2015) 564–573.
[11] Y. Ma, et al., Nanoindentation study on shear transformation zone in a CuZrAl metallic glassy film with different thickness, J. Non-Cryst. Solids 442 (2016) 67–72.
[12] R.A. Sergiienko, et al., Thermophysical properties of Zr65Cu17.5Ni10Al7.5 bulk metallic glass, J. Non-Cryst. Solids 652 (2025) 123400.
[13] J. Zhang, et al., Fe-based bulk metallic glass with high thermal stability and corrosion resistance, J. Non-Cryst. Solids 643 (2024) 123176.
[14] S. Yang, et al., Enhanced mechanical properties and biocompatibility of a Ti-Zr-Cu-Pd bulk metallic glass by annealing within the supercooled liquid region, J. Alloy. Compd. 1010 (2025) 178081.
[15] G. Wang, et al., Friction joining of Ti40Zr25Ni3Cu12Be20 bulk metallic glass, J. Mater. Process. Technol. 212 (9) (2012) 1850–1855.
[16] Z. Jamili-Shirvan, et al., Microstructure characterization and mechanical properties of Ti-based bulk metallic glass joints prepared with friction stir spot welding process, Mater. Des. 100 (2016) 120–131.
[17] Z. Jamili-Shirvan, et al., Thermal behavior and non-isothermal crystallization kinetics of (Ti41Zr25Be28Fe6) 93Cu7 bulk metallic glass, J. Non-Cryst. Solids 447 (2016) 156–166.
[18] J.T. Kim, et al., Plastic deformation behavior of Fe–Co–B–Si–Nb–Cr bulk metallic glasses under nanoindentation, J. Alloy. Compd. 587 (2014) 415–419.
[19] X. Wang, et al., Nanoindentation study on the room temperature creep characteristics of a senary Ti16. 7Zr16. 7Hf16. 7Cu16. 7Ni16. 7Be16. 7 high entropy bulk metallic glass, J. Non-Cryst. Solids 470 (2017) 27–37.
[20] J. Pi, et al., Nanoindentation mechanical properties of glassy Cu29Zr32Ti15Al5Ni19, J. Alloy. Compd. 657 (2016) 726–732.
[21] C. Schuh, T. Nieh, A nanoindentation study of serrated flow in bulk metallic glasses, Acta Mater. 51 (1) (2003) 87–99.
[22] S. Jha, et al., Structural and stress state dependence of small-scale deformation in bulk metallic glass, J. Alloy. Compd. 961 (2023) 170971.
[23] W. Huo, et al., Thermodynamic and kinetic investigation on crystallization of photosensitive glass-ceramics via molecular dynamics, J. Non-Cryst. Solids 649 (2025) 123332.
[24] Z. Lulu, et al., Molecular dynamics simulations study on structure and mechanical properties of Na2O–CaO-Al2O3-B2O3-SiO2 glasses with different Al2O3/B2O3 ratio, J. Non-Cryst. Solids 641 (2024) 123154.
[25] S. Bogtob, et al., Effect of Ni-reinforcement size on mechanical properties of Al metallic glass matrix from molecular dynamics, J. Non-Cryst. Solids 646 (2024) 123211.
[26] Y.-L. Li, et al., Molecular dynamics simulation of shock-induced plastic deformation and spallation behavior of Cu/Cu64Zr36 crystalline/amorphous composites, J. Non-Cryst. Solids 647 (2025) 123300.
[27] Y. Wang, H. Song, Abnormal indentation behavior of amorphous/crystalline dual-phase Mg alloys: a molecular dynamics simulation, J. Non-Cryst. Solids 646 (2024) 123241.
[28] Y. Luo, et al., The effect of crystalline structure on the mechanical behavior in Zr-based amorphous materials: a molecular dynamics simulation, J. Non-Cryst. Solids 622 (2023) 122667.
[29] M. Celtek, S. Sengul, U. Domekeli, Glass formation and structural properties of Zr50Cu50-xAlx bulk metallic glasses investigated by molecular dynamics simulations, Intermetallics 84 (2017) 62–73.
[30] A. Annamareddy, et al., Mechanisms of bulk and surface diffusion in metallic glasses determined from molecular dynamics simulations, Acta Mater. 209 (2021) 116794.
[31] O. Adjaoud, K. Albe, Microstructure formation of metallic nanoglasses: insights from molecular dynamics simulations, Acta Mater. 145 (2018) 322–330.
[32] S. Verma, P. Sarkar, P. Pant, Thermal drift in room temperature nanoindentation experiments: measurement and correction, J. Mater. Res. 36 (2021) 3436–3444.
[33] M. Celtek, Atomic structure of Cu60Ti20Zr20 metallic glass under high pressures, Intermetallics 143 (2022) 107493.
[34] S. Xu, et al., Molecular dynamics simulations of nano-indentation and wear of the γTi-Al alloy, Comput. Mater. Sci. 110 (2015) 247–253.
[35] Y. Tian, Q. Fang, J. Li, Molecular dynamics simulations for nanoindentation response of nanotwinned FeNiCrCoCu high entropy alloy, Nanotechnology 31 (46) (2020) 465701.
[36] Q. Fang, et al., Deformation behaviors of Cu29Zr32Ti15Al5Ni19 high entropy bulk metallic glass during nanoindentation, Appl. Surf. Sci. 443 (2018) 122–130.
[37] X. Zhou, R. Johnson, H.N. Wadley, Misfit-energy-increasing dislocations in vapor-deposited CoFe/NiFe multilayers, Phys. Rev. B 69 (14) (2004) 144113.
[38] X. Wang, et al., Optimizing Ni-Zr-Ti metallic glasses: Cluster design and molecular dynamics evaluation of glass forming ability, J. Alloy. Compd. 1009 (2024) 177007.
[39] C. Feng, et al., Molecular dynamics simulation of nano-indentation on Ti-V multilayered thin films, Phys. E Low-dimens. Syst. Nanostruct. 87 (2017) 213–219.
[40] W.-H. Wang, H.Y. Bai, Role of small atoms in the formation and properties of Zr–Ti–Cu–Ni–Be bulk amorphous alloys, J. Appl. Phys. 84 (11) (1998) 5961–5968.
[41] J. Lv, et al., The molecular dynamic simulation on impact and friction characters of nanofluids with many nanoparticles system, Nanoscale Res. Lett. 6 (2011) 1–8.
[42] S.L. Mayo, B.D. Olafson, W.A. Goddard, DREIDING: a generic force field for molecular simulations, J. Phys. Chem. 94 (26) (1990) 8897–8909.
[43] C.-H. Wang, et al., Investigations of the mechanical properties of nanoimprinted amorphous Ni–Zr alloys utilizing the molecular dynamics simulation, J. Alloy. Compd. 659 (2016) 224–231.
[44] F. Pöhl, Determination of unique plastic properties from sharp indentation, Int. J. Solids Struct. 171 (2019) 174–180.
[45] H. Vafaeenezhad, et al., Flow behavior and strain rate sensitivity assessment of γ and γ′ phases in Co–Al–W-based superalloy using experimental and computational approaches, J. Mater. Res. Technol. 18 (2022) 4617–4630.
[46] S. Goel, et al., Molecular dynamics simulation of nanoindentation of Fe3C and Fe4C, Materials Science Engineering A 597 (2014) 331–341.
[47] A.P. Thompson, et al., LAMMPS-a flexible simulation tool for particle-based materials modeling at the atomic, meso, and continuum scales, Comput. Phys. Commun. 271 (2022) 108171.
[48] R. Ando, et al., Analysis of nano-hardness distribution near the ferrite-martensite interface in a dual phase steel with factorization of its scattering behavior, ISIJ Int. 61 (1) (2021) 473–480.
[49] G. Wu, et al., Elemental partitioning-mediated crystalline-to-amorphous phase transformation under quasi-static deformation, Nat. Commun. 15 (1) (2024) 1223.
[50] B. Adam, et al., Introduction of sulfur into an eutectic of the Zr-Ti-Ni-Cu system: alloy development and characterization of the (Zr50Ti16. 6Ni18. 3Cu15) 100-xSx bulk metallic glasses, J. Alloy. Compd. (2025) 180307.
[51] H. Vafaeenezhad, et al., Nanomechanics of Mg-Gd-Y-Nd-Zn alloy with LPSO and MgRE phases, J. Magnes. Alloy. 12 (8) (2024) 3370–3393.
[52] X. Zhu, et al., Effect of strain rate on nano-scale mechanical behavior of A-Plane (11 2^{-} 0) ZnO single crystal by nanoindentation, Micromachines 14 (2) (2023) 404.
[53] Y. Zhao, et al., Size-dependent microstructural evolution and mechanical properties of crystalline/amorphous high-entropy alloy nanostructured multilayers: Cu/FeCoCrNiBSi vs Ni/FeCoCrNiBSi, Acta Mater. 246 (2023) 118706.
[54] H. Wang, et al., Strain rate sensitivity in Zr-based metallic glass: experiments and molecular dynamics study, J. NonCryst. Solids 605 (2023) 122168.
[55] M.A. Zeeshan, et al., Electrochemically synthesized amorphous and crystalline nanowires: dissimilar nanomechanical behavior in comparison with homologous flat films, Nanoscale 8 (3) (2016) 1344–1351.
[56] H. Guo, et al., Tensile ductility and necking of metallic glass, Nat. Mater. 6 (10) (2007) 735–739.